Applied Surface Science 636 (2023) 157799

Contents lists available at ScienceDirect

Applied Surface Science

journal homepage: www.elsevier.com/locate/apsusc

Full Length Article

Polydiacetylene-coated gold nanoparticles as a novel plasmonic thermosensor based on the phase transition of the outer shell

Marianna Pannico [a], Pellegrino Musto [a,*], Marina Alloisio [b,*], Andrea Dodero [c], Maila Castellano [b], Silvia Vicini [b]

[a] Institute for Polymers, Composites and Biomaterials, National Research Council of Italy (CNR-IPCB), Pozzuoli (Naples), Italy
[b] Department of Chemistry and Industrial Chemistry, University of Genoa, Via Dodecaneso 31, 16146 Genoa, Italy
[c] Adolphe Merkle Institute, University of Fribourg, Chemin des Verdiers 4, 1700 Fribourg, Switzerland

ARTICLE INFO

Keywords:
Core–shell nanoparticles
SERS
Polydiacetylenes
Thermosensors
Ultrathin films

ABSTRACT

We report the synthesis of a core–shell nanostructure formed by a gold nanosphere surrounded by an external layer of poly(10,12-pentacosadiynoic acid). The gold core provides intense SERS signaling, whereas the polymer shell ensures structure stability. We introduce the concept of temperature response induced by phase-transition, as opposed to current plasmonic thermosensors based on surface adsorption of low molecular weight reporters. The behavior of the core–shell nanostructure has been investigated by Variable Temperature SERS (VT-SERS) measurements in the range of 150 – 400 K. The polymer shell is initially in the blue form and converts into the stable red one starting from 290 K. This transition produces temperature effects on the position and the Full Width at Half Height (FWHH) of the ν(–C = C–) peak that are suitable for temperature monitoring. VT-SERS measurements are proved to be useful for studying the behavior of ultrathin polymer films.

1. Introduction

Nanotechnology is at the forefront of contemporary research; its advent has generated new paradigms and challenges on both the theoretical and the experimental side. In this context, plasmonic nanoparticles (PNPs) play a central role: they find application in energy harvesting, catalysis, nanomedicine, and numerous other fields [1]. Absorption of visible light by these nanoobjects leads to the formation of *hot electrons*; these can be emitted in the surroundings or may remain trapped inside the nanoparticles causing local heating. In the presence of molecules adsorbed on the metal surface, *hot electrons* may also interact with the adsorbate inducing photochemistry. Important reactions like water splitting [2,3], H_2 dissociation [4], and alkene epoxidation [5,6] can be promoted in mild conditions on active plasmonic surfaces. In nanomedicine, the recently emerged field of plasmonic phototherapy relies on the heat generated by irradiating PNPs that are selectively incubated in tumor cells [7]. A further application is intracellular temperature mapping [8,9]: the pathogenesis of numerous diseases, including cancer, is characterized by exceptional heat production. An accurate, contactless temperature monitoring inside cells is crucial for diagnostic purposes. PNPs are ideal candidates to achieve this goal since they can be readily internalized in cells and subcellular structures [7,10,11]. In all these cutting-edge applications, for a fundamental understanding and an intelligent design of the nanostructures, it is essential to identify and quantify the thermoplasmonic effect, i.e. the heat generated by the resonance process at the place where it is produced, that is at the PNP surface and/or at the so-called hot-spots (1–5 nm gaps at inter-particle junctions) [12,13]. This requires the remote monitoring of the temperature distribution at the nanoscale. Numerous optical techniques have been suggested for this purpose, including infrared, Raman, UV/VIS, and fluorescence, but all of them are restricted to the diffraction limit. Surface Enhanced Raman Scattering (SERS) is an attractive tool for such application because the SERS and the plasmonic photothermal effects can be excited simultaneously. However, the power density required to boost a significant number of hot-electrons from the Fermi level is usually much larger than the threshold value for inducing detectable SERS signaling, which makes it possible to decouple the two processes when calibrating the response function against the temperature of the surrounding medium [8]. This is to be carefully verified case by case if meaningful working curves are to be produced. A further advantage of SERS spectroscopy is represented by the enormous enhancement of the Raman cross-section for specific

* Corresponding authors.
E-mail addresses: pellegrino.musto@cnr.it (P. Musto), marina.alloisio@unige.it (M. Alloisio).

https://doi.org/10.1016/j.apsusc.2023.157799
Received 7 April 2023; Received in revised form 29 May 2023; Accepted 14 June 2023
Available online 17 June 2023

peaks, induced by plasmonic resonance. In general, the signal may increase by a factor between 10^5 and 10^8 with respect to spontaneous inelastic emission, providing a sensitivity suitable for nanoscale sampling. The large signal enhancement is mainly generated at the hotspots (typically, around 85% of the SERS signal is contributed by 6% of molecules residing therein [14]), which provides the required spatial resolution (less than 10 nm).

A number of studies have been published on the development of SERS thermosensors. The first report on the use of Ag/Au PNPs as room temperature sensors dates back to 2014 [15]. Using the Rhodamine dye as a molecular reporter, variable-temperature SERS (VT-SERS) measurements demonstrated a linear *intensity* vs *T* relationship in the range 25–45 °C; the behavior was reversible over at least 25 cycles for Au and 15 cycles for Ag, which warrants reusability. A slope of the response function of ca. 430 counts • s^{-1}/°C provided an excellent sensitivity. In a successive contribution [8], the choice of SERS intensity was questioned on the basis of the multiplicity of effects that temperature may have over spontaneous and/or plasmon-enhanced scattering. Instead, it was proposed to use the peak frequency of selected signals because this parameter was considered more robust and less dependent on operating conditions. In that case, the molecular reporter was phenyl isocyanide on gold PNPs, which provided a sensitivity of 0,232 cm^{-1}/°C. The SERS thermosensor was validated by monitoring the laser-induced desorption of CO on gold PNPs and by intracellular thermometry of a single living cell [8]. A very recent publication [16] focused on the sensitivity optimization of a SERS thermosensor. It was demonstrated that the type of chemical bond of the probe molecule and the interaction mechanism with the metal surface are the key factors ruling the frequency-temperature function. Thus, the sensitivity follows the sequence triple bond > double bond > single bond for both aliphatic and aromatic probes, while the surface chemical bonding effect substantially increases the temperature dependence of the peak position [16].

All the SERS thermosensors proposed so far rely on the response of a molecular reporter adsorbed on the PNP surface. This approach suffers from a number of drawbacks: i) in the explored temperature range partial or even complete desorption of the probe may occur, affecting both the sensitivity and the working range of the sensor; ii) in aggressive environments the SERS reporter may be replaced by more reactive molecules, especially when the probe is physisorbed rather than chemisorbed; iii) in complex media rich in reactive components, such as the cellular environment, the functional groups providing temperature sensitivity may react/interact, resulting in severe modifications of the response function.

In the present contribution, we propose an alternative approach to SERS thermosensing, intended to respond to the above issues. We have synthesized a composite plasmonic nanostructure with an inner core formed by a gold nanosphere having a diameter of around 15 nm and a polymeric external shell made of poly(10,12-pentacosadiynoic acid (pPCDA). Polymer coated plasmonic nanoparticles have been already reported in the literature and proposed for biomedical applications [17,18]. The novel polydiacetylene-stabilized gold PNPs (pPCDA@AuNPs) have been prepared following a three-step approach previously set up to produce core–shell nanohybrids in water [19,20]. In the resulting nanostructures, the gold core provides excellent plasmonic properties producing an intense and well-resolved SERS spectrum. Furthermore, the *in-situ* polymerized external layer is permanently bound to the inner nanosphere, which guarantees robustness and stability of the structure up to the degradation temperature of the polymer shell (above 300 °C) [21]. In this situation, the response function no longer depends on the surface chemistry, nor the reactivity of the surrounding medium, but only on the behavior of the polymer shell as a function of temperature. This has allowed us careful control and improved reproducibility of the VT-SERS effect. We have investigated the behavior of pPCDA@AuNPs as a function of temperature in the 150–400 K range, when the polymer shell is initially in the blue-form and converts into the red-form towards the upper end of the temperature interval. The occurrence of multiple phase transitions was detected via VT-SERS and it was shown that both the position and the Full Width at Half Height (*FWHH*) of a specific peak are suitable parameters for temperature monitoring. The intensity is also sensitive to temperature changes but displays a complex behavior reflecting the phase transitions. The results presented herein also demonstrate that VT-SERS is a promising experimental approach for studying the behavior of ultrathin polymer films up to the single macromolecular layer.

2. Experimental

2.1. Reagents, solvents, and glassware

Chemicals and spectroscopic grade solvents were commercial products used as received, except the diacetylene monomer 10,12-pentacosadiynoic acid (PCDA, Sigma-Aldrich), which was purified prior to use from the spontaneously formed blue polymer by means of dissolution in ethanol followed by filtration with 0.20-μm PTFE syringe filter. Aqueous solutions were prepared with ultra-high-purity Milli-Q water distilled twice prior to use. Before the synthesis of the nanostructures, the glassware was thoroughly cleaned with freshly "piranha" (mixture of cooled 30% v/v hydrogen peroxide and concentrated sulfuric acid in a ratio of 1:2 v/v) and then rinsed with bi-distilled water for immediate use.

2.2. Synthesis of CTAB-stabilized gold nanoparticles

Gold nanoparticles stabilized with cetyl-trimethyl ammonium bromide (CTAB), CTAB@AuNPs, were prepared through a standard wet chemical approach carried out at room temperature. In detail, in a cleaned glass flask $HAuCl_4$ (1 mL, 0,1 mol/L) was added to 100 mL of bi-distilled water and then reduced with a freshly prepared aqueous solution of $NaBH_4$ (5 mL, 0,2 mol/L) in the presence of CTAB (2 mL, 0,2 mol/L) acting as a stabilizer. The solution, which immediately became a deep red suspension, was maintained under stirring for approximately 24 h to complete. The crude product of the nominal concentration of 1 mmol/L in terms of Au content was purified from the CTAB excess by filtration with a paper filter followed by centrifugation at 14,5k rpm for 10 min, re-dispersed in water and then stored at room temperature. Color changes and stability of the sample were constantly monitored by means of UV–Vis spectroscopy.

2.3. Synthesis and polymerization of PCDA-coated gold nanoparticles

Gold nanoparticles coated with PCDA molecules (PCDA@AuNPs) were obtained by chemisorption of the diacetylene on as-prepared CTAB@AuNPs properly modifying a ligand-exchange reaction (LER) protocol set up to produce core–shell nanoparticles in water [19,22]. To ensure the anchorage of PCDA molecules, the CTAB-protected precursors were previously treated with an aqueous solution of $NaBH_4$, following a published procedure [23]. In detail, 8 mL of a freshly prepared aqueous solution of $NaBH_4$ (50 mml/L) were added to 8 mL of hydrosol containing the purified CTAB@AuNPs; the mixture was left for 1 h under stirring at room temperature and then added by 0.75 mL of PCDA dissolved in ethanol (7 mmol/L). The diacetylene addition was portion wised in three aliquots of 0.25 mL every hour to avoid spontaneous micellization of PCDA. The mixture was maintained for a day in the dark at room temperature under constant stirring to allow the reaction to complete. Afterward, the sample was placed in a fused silica cuvette and subjected to UV light for 1 min in a Rayonet chamber (254 nm and 35 W) to induce the photopolymerization of the diacetylene shell. The crude polymerized nanoparticles were then purified from micelles of poly(PCDA) (pPCDA) and aggregates by centrifugation at 8 k rpm for 15 min followed by filtration under vacuum with a 1,2 μm glass-fiber filter. In this way, clean pPCDA@AuNPs hydrosols were obtained and stored in the dark at room temperature. Continuous monitoring by

UV–Vis spectroscopy revealed that the resulting aqueous suspension containing pPCDA@AuNPs is stable for months.

2.4. Characterization of PNPs

Electronic absorption spectra of colloidal suspensions were recorded at room temperature through a Shimadzu UV-1800 spectrophotometer with fused silica cuvettes of different pathlengths.

Field Emission Scanning Electron Microscopy (FESEM) images were acquired by a ZEISS SUPRA 40 VP microscope operating at 20 keV in both direct (InLens mode) and back (QBSD mode) configurations. Before the morphological characterization, the samples were sputter-coated with carbon using a Polaron E5100 sputter coater to obtain good conductivity. A statistical analysis of the nanoparticle features was carried out on at least 100 measurements, taken from FESEM images at different magnifications with the open-source software Image J, as detailed in a previous work [24].

2.5. Sers measurements

The spectra were collected by a confocal Raman micro spectrometer (XploRA-Plus, Horiba-Scientific, Japan) with a 638,2 nm diode laser as the exciting source and an Edge filter for recording the Stokes scattering down to 50 cm^{-1}. The radiation was collected by an Olympus metallurgical objective with a 10x magnification and a numerical aperture of 0.25, resulting in a laser spot size of 3 μm. The confocal and slit apertures were set to 500 and 200 μm, respectively. A grating with 1800 grooves/mm was used to disperse the scattered light with the highest spectral resolution. The radiation was focused onto a CCD detector (Horiba Cameras, Mod. Syncerity,) cooled at − 65 °C by a Peltier module; it was operated in the Raman-shift range 400 – 2500 cm^{-1}. The full laser power measured at the output of the objective was 25.4 mW; all measurements were carried out with a 25% nominal attenuation, corresponding to 6.9 mW; the exposure time was 2 s. The spectra were calibrated using a monocrystalline silicon wafer as reference (primary Raman mode at 520 cm^{-1}). Temperature measurements were carried out under an inert atmosphere (dry N_2, flow rate 150 mL/min) in a Linkam cell Mod. THMS350V (Surrey, UK) with electrical temperature control in the range between −180 and 350 °C (accuracy = ± 0,1°C).

The Raman imaging measurement in the mapping mode was performed by placing the sample on a piezo-electrically driven microscope stage with an *x,y* resolution of 10 ± 0,5 nm and a *z* resolution of 15 ± 1 nm. The stage was scanned at a constant speed in the *x–y* plane over a 2350 × 2350 μm area with a 5.0 μm step size. A *z*-scan was also performed with the same experimental setup between −15 and 15 μm relative to the optical focus, with a step size of 0.5 μm.

Bandshape analysis in the 1350 – 1550 cm^{-1} was performed by a least squares curve fitting (LSCF) algorithm based on the Levenberg-Marquardt method [25,26]. The model for the simulation of the experimental profiles employed a mixed Gauss-Lorentz lineshape with three components:

$$A(\nu) = \sum_{i=1}^{3} \left\{ (1 - L_i) H_i \ exp\left[- ln2 \left(\frac{\nu - \nu_{0,i}}{a_i} \right)^2 \right] + L_i \frac{H_i}{1 + \left(\frac{\nu - \nu_{0,i}}{a_i} \right)^2} \right\} \quad (1)$$

where ν is the frequency (cm^{-1}), $H_i$and $\nu_{0,i}$ are, respectively, the height and the position of the *ith* component, L_i is the Lorentz factor ($0 \leq L_i \leq 1$) and a_i is the half width at half height ($FWHH_i/2$). The adopted model was able to simulate the experimental profiles with high accuracy (average coefficient of determination, R^2, = 0.997; average standard error = 90; see *Fig. 6S, Supplementary Material (SM)*) in the whole temperature range investigated. The LSCF analysis allows us to improve the accuracy of the band parameters $\nu_{0,i}$ and $FWHH_i$ by using all the data points of the profile (225); the accuracy achieved by LSCF is estimated to be 0.1 cm^{-1}, while is 0.5 cm^{-1} by direct evaluation on the raw data.

3. Results and discussion

3.1. Synthesis and characterization of the PNPs

The core–shell nanostructures were obtained in three steps: first, gold nanospheres stabilized with cetyltrimethylammonium bromide (CTAB@AuNPs) were synthesized by means of a standard wet protocol [27]. Secondly, the as-prepared CTAB@AuNPs were incubated with a PCDA aqueous solution to allow the chemisorption of the carboxyl-substituted diacetylene on the gold nanoparticle surface by means of a ligand-exchange reaction (LER). Once obtained, the PCDA-coated gold nanoparticles (PCDA@AuNPs) were irradiated with UV light to induce the polymerization of the outer diacetylene shell directly in an aqueous suspension (pPCDA@AuNPs).

High-resolution FESEM images of CTAB@AuNPs precursors are reported in Fig. 1a together with the UV–Vis spectra of the corresponding hydrosol (Fig. 1b). The main geometrical parameters extracted by the FESEM images are listed in Table 1.

Based on the data reported, the sample is mainly constituted of nearly spherical particles of about 30 nm diameter with limited size dispersion (Fig. 1S in SM) and shape yield around 80%. Larger pseudo-nanospheres with an average diameter slightly more than doubled together with short nanorods with an axial ratio of around 2 and triangularly shaped nanoparticles with an average edge length of about 50 nm are also present in small percentages as byproducts (Fig. 1S, 2S, 3S in Supplementary Material).

The low size and shape heterogeneity of CTAB@AuNPs is confirmed by the spectral profile of the corresponding hydrosol, also reported in Fig. 1. Indeed, the spectrum is dominated by a sharp band centered at 526 m, corresponding to the typical surface plasmon resonance (SPR) band of isotropic and low polydispersed gold nanoparticles.

As indicated above, CTAB@AuNPs were used as substrates for PCDA assembly to form core–shell nanoparticles (PCDA@AuNPs), which in turn were exposed to UV light to induce the photogeneration of the polydiacetylene layer (pPCDA@AuNPs). The resulting products were morphologically and spectroscopically investigated to ascertain the reaction success (Fig 2). As before, the main geometrical parameters extracted by the FESEM images are also listed in Table 1.

The results of the FESEM characterization of dried pPCDA@AuNPs, carried out in both direct and back-scattered modes to discriminate the more reflective gold cores from the polydiacetylene shells, are shown in Fig 2a. The images highlight the core–shell architecture of the nanoparticles, as expected. In detail, the inner gold cores have spherical-like geometry and an average diameter of about 15 nm, whereas the outer polymeric covering has an average thickness of 12,7 nm. According to a model of molecular mechanics reported in literature [19], the PCDA arrangement around the AuNPs occurs by subsequent stratification of bilayers on the metal surface; each bilayer is 6,264 nm thick. Based on these assumptions, the polymeric shell of pPCDA@AuNPs is on average made up of two superimposed bilayers of diacetylene molecules. As far as the core size is concerned, the diameter value reported in Table 1 is about halved with respect to that of the corresponding precursors. This result is consequent to the purification process of the crude sample, which led to the selection of the smallest and least polydispersed nanoparticles (Fig. 4S in SM).

The supramolecular architecture of pPCDA@AuNPs is also confirmed by monitoring with UV–Vis spectroscopy. Fig. 2b shows the spectra recorded before (pink line) and after (black line) exposure to UV light. The pink profile, corresponding to PCDA@AuNPs hydrosol, is characterized by a well-defined SPR at around 540 nm. The plasmon band appears enlarged and red-shifted with respect to that of CTAB@AuNPs precursors because of the chemical changes induced on the metal core surface by PCDA chemisorption, as previously observed [19]. The spectrum of pPCDA@AuNPs hydrosol (black line) exhibits a more

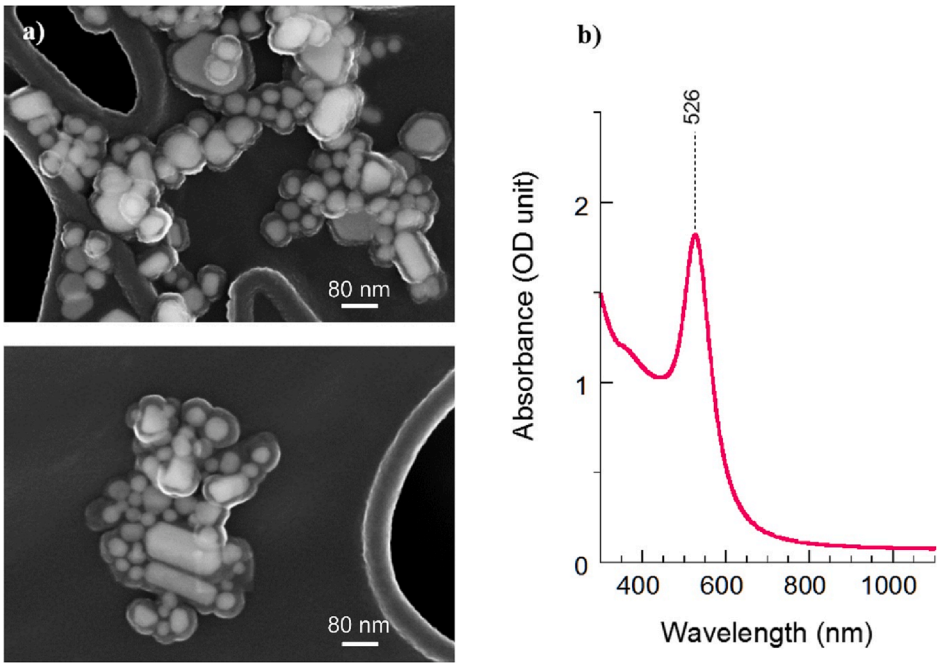

Fig. 1. a) FESEM images of CTAB@AuNPs recorded in direct configuration; **b)** UV–Vis spectrum of CTAB@AuNPs hydrosol.

Table 1
Geometrical parameters of CTAB@AuNPs and pPCDA@AuNPs extracted from FESEM images of Fig. 1 and Fig. 2, respectively.

Sample	%	Diameter (nm)	Length (nm)	axial ratio
CTAB@AuNPs	79	28.1 ± 0.5 (6.5)	–	1.3 (0.3)
nanospheres	8	65 ± 4 (16)	–	1.2 (0.2)
CTAB@AuNPs	7	35 ± 3 (12)	72 ± 10 (37)	2.0 (0.6)
nanorods				
CTAB@AuNPs	6	–	48 ± 3 (12)	–
nanotriangles				
pPCDA@AuNPs	–	15 ± 1 (5)	–	1.3 (0.3)
cores				
pPCDA@AuNPs	–	–	12.7 ± 0.8 (5.1)	–
shell				

The standard deviation of values is reported in brackets.

structured lineshape, consisting of a sharp band centered at 650 nm and an absorptions envelope in the 500–600 nm spectral interval. The first one corresponds to the excitonic peak assigned to blue polydiacetylenes, whereas the second one is the result of the superimposition between the first vibrational side-band of the poly(PCDA) at around 592 nm and the SPR band of the gold cores at around 540 nm. Point-to-point subtraction of the spectrum of PCDA@AuNPs to that of pPCDA@AuNPs yielded the blue line of Fig. 2, which actually corresponds to that of a polydiacetylene in its "pure" highly conjugated blue form, suitable for nonlinear and sensing purposes [19,20].

A schematic representation of the formation and subsequent photopolymerization of a single and double PCDA bilayer around a gold nanosphere is reported in Fig. 3.

3.2. VT-SERS experiments

The VT-SERS measurement was performed on a round-shaped spot obtained by deposition on an Aluminum substrate, of 2 μL of the PNP colloidal solution. Raman imaging at room temperature of the drop-cast spot is represented in Fig. 4, where the image reconstruction was made by considering the intensity of the 1447 cm^{-1} peak (peak frequency refers to the value at 301 K if not otherwise specified). It is found that the adopted drop-casting procedure produces a macrospot having a 2,310 ± 5 μm diameter; the SERS activity is intense and uniformly distributed across the whole spot area and the spectrum is very consistent.

The localized surface plasmon resonances (LSPR) of the PNPs are responsible for both enhanced light scattering and enhanced light absorption. Scattering (inelastic) generates the SERS effect while the absorbed power, Q, is delivered as heat according to the general relationship: $Q = \sigma_{abs} I$, where σ_{abs} is the absorption cross-section and I is the Irradiance, i.e. the power density of the exciting beam ($W/\mu m^2$). Thus, the heating effect is ruled by the value of σ_{abs}, which, for spherical PNPs, depends strongly on the particle diameter: it is negligible up to 35 nm, while increasing exponentially up to 60×10^3 nm^2 at a particle diameter of 120 nm [28]. To avoid heating effects during the SERS experiment, which would impair the response functions, we purposely synthesized composite nanoparticles with an inner diameter of 15 nm. Measurements as a function of the irradiation power and time were performed to confirm the stability of the local temperature (and the associated spectral response) at the laser spot.

The results (see Fig. 5) indicated that the band parameters (position and *FWHH*) remain invariant in a laser power range (at sample) between 0.09 and 25.4 mW and – irradiating at 6.92 mW – for exposure times between 0.5 and 9 s. It is expected that heat generation at the PNP surface will be strongly enhanced for inner particle sizes exceeding 40 nm [8]. The thermo-plasmonic effect is currently under investigation as a function of particle size and shape and the results will be presented in a forthcoming contribution.

The SERS spectra collected at different temperatures at point A of Fig. 4 are displayed in Fig. 6, while Table 2 summarizes the peak frequencies and their tentative assignments. The SERS spectra are essentially coincident with their Raman counterparts, both in terms of peak position and relative intensity of the various components [29]. This indicates that the functional groups responsible for the prominent signals [(–C≡C–, –C = C–, CH_2] experience the electromagnetic (EM) resonance effect but are not directly bound to the metal surface, which would cause significant peak shift/broadening. In fact, the interaction with the metal surface is assumed to occur through the carboxylic acid groups of the $(CH_2)_8COOH$ substituent (see Fig. 3). In this arrangement, according to semi-empirical *QM* simulations [19], the first polymer backbone and the $(CH_2)_{11}CH_3$ substituent are located about 1.5 nm from

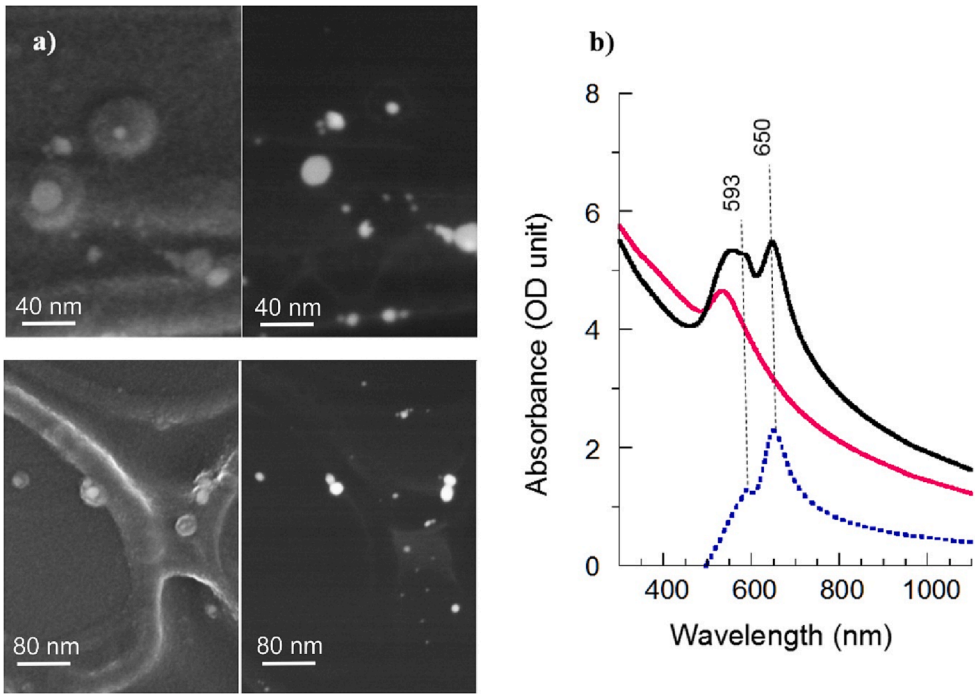

Fig. 2.A.) FESEM images of pPCDA@AuNPs recorded in direct (*left*) and back-scattered (*right*) configurations at two different magnifications; **b)** UV–Vis spectra of the hydrosols of PCDA@AuNPs (pink line) and pPCDA@AuNPs (black line); the dotted blue line corresponds to the point-to-point difference spectrum. (For interpretation of the references to color in this figure legend, the reader is referred to the web version of this article.)

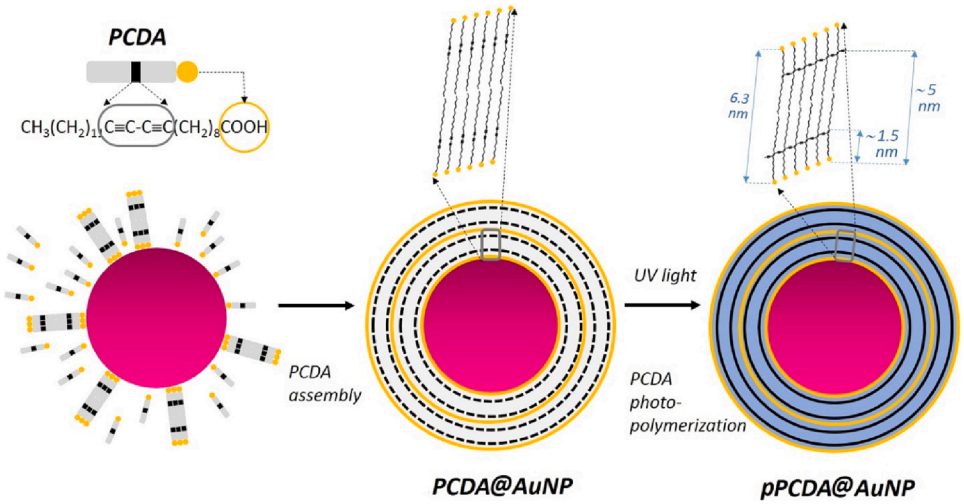

Fig. 3. Schematic representation of the self-assembling process leading to PCDA@AuNP and the subsequent photopolymerization of the PCDA bilayer.

the PNP surface, which warrants the EM plasmonic effect to occur, since on gold surfaces it vanishes exponentially at a distance of around five nm [30]. The characteristic sequence of CH_2 wagging vibrations due to the phase difference between adjacent methylene groups (k = 1 to 5) confirms that the alkyl substituents of the pPCDA shell retain the *all-trans* conformation observed in the bulk blue form [29]. The low-temperature SERS pattern verify that the pPCDA shell is in the pure blue form as the peaks of the red form (2122, 1513 cm^{-1}) are barely detectable. It is found that from 133 to 300 K the spectrum changes slightly, while at 373 K the overall intensity decreases substantially and a shift/broadening of several peaks becomes apparent. The VT-SERS measurement has been performed in the temperature range 133 – 415 K because above this interval the blue-to-red transition is essentially complete. This is shown in Fig. 7, which reports the sequence of SERS spectra in the blue-to-red transition interval (373 – 415 K).

We focused our analysis on the ν(–C = C–) range between 1350 and 1620 cm^{-1}, the evolution of which with temperature is illustrated in the inset of Fig. 7. This choice is suggested by the substantial intensity of the signal and the well-behaved bandshape (a symmetrical profile that is reliably simulated by standard shape-functions [26], see Fig. 6S in SM). In the inset of Fig. 7, the band profile has been normalized over the maximum intensity; this alternative representation allows an easier comparison among the spectra by compensating for the large intensity drop. The plot highlights the upward shift and the line broadening of the blue-form peak at 1447 cm^{-1} as the temperature increases, and its gradual conversion in the component at 1512 cm^{-1}, characteristic of the red-form. The latter becomes predominant starting from 408 K.

The position and the *FWHH* of the ν (–C = C–) vibration of the blue-

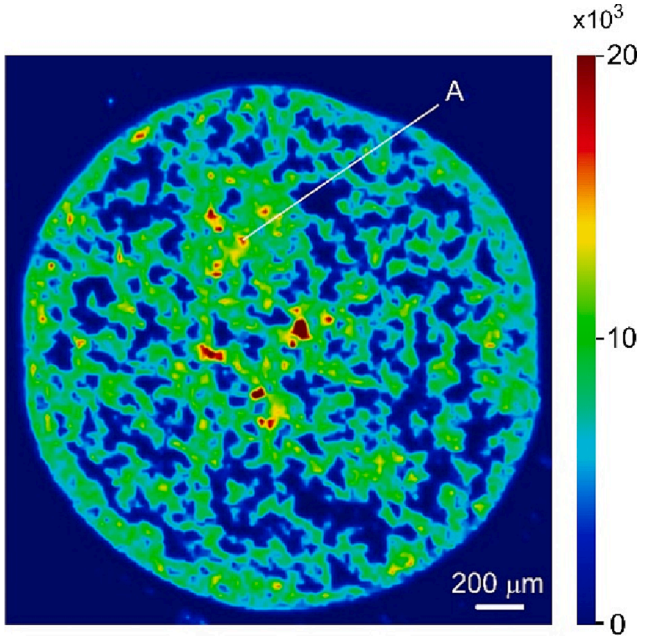

Fig. 4. Drop-casting of 2 μL of a PNPs colloidal solution on an Aluminum substrate. Raman image obtained by considering the intensity (peak height) of the 1447 cm^{-1} signal.

form are reported as a function of temperature in Fig. 7a-b, respectively. In the range of 150 – 358 K the observed behavior conforms to the predictions of the theory for a system undergoing an order/disorder transition [31–34]. In fact, it has been demonstrated that for a simple harmonic oscillator, which represents a reasonable approximation for the present ν (–C = C–) mode, the relationship between the peak frequency, ν, and the temperature assumes the form [35]:

$$\nu^2 = \nu_0^2\ [1 + \gamma(T - T_c)\,] \qquad (2)$$

where ν_0 is the so-called 'hard-core frequency' at T_c and γ is the thermal expansion coefficient. In general, γ is phase dependent, which causes an abrupt change of slope in the linear ν^2 vs T diagram at the phase transition. This is what is observed in the present case at T_c = 290 K. Regressing eq. (2) against the experimental data (see inset of Fig. 8a) provides a ν_0 value of 1446.3 cm^{-1} and an expansion coefficient of 16.3 × 10^{-6} K^{-1} for $T < T_c$, which becomes 67.1 × 10^{-6} K^{-1} (ν_0 = 1446.2 cm^{-1}) for $T_c < T < 358$ K. For comparison, the expansion coefficients of polystyrene, poly(ethylene terephthalate), polypropylene and polyethylene are, respectively, 70, 59, 72–90 and 108–200 × 10^{-6} K^{-1}. The phase transition detected by the VT-SERS measurement at 290 K is

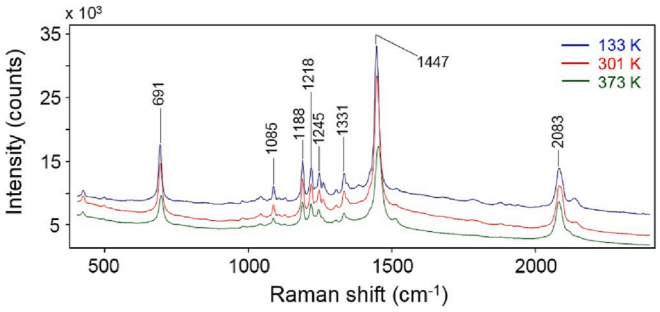

Fig. 6. SERS spectra collected at point A of Fig. 4 at temperatures as indicated.

related, in our view, to the activation of the molecular mobility of the aliphatic substituents, while the backbone chain remains unaffected. This conclusion is supported by the observation that up to 358 K the peaks characteristic of the red-form, originating from a conformational rearrangement of the main chain, do not emerge (*vide infra*). The intensity of these peaks starts to increase above 360 K, a temperature corresponding to a second change of slope in the ν^2 vs T diagram (see inset of Fig. 8a), which likely corresponds to a further phase transition mainly involving the backbone chain.

When the γ value is sufficiently small eq. (2) can be approximated by:

Table 2
Observed peak frequencies and tentative assignments for the SERS spectrum collected at 301 K on the pPCDA@AuPNPs in the blue form.

Frequency (cm^{-1})	Tentative assignment
2138 *sh, w*	–
2083 *s*	ν(–C≡C–)
1447 vs	ν(–C = C–)
1343 *sh*	–
1331 *m*	CH_2 wag; k = 5
1304 *w*	CH_2 wag; k = 4
1258 *m*	–
1245 *m*	CH_2 wag; k = 3
1218 *m*	CH_2 wag; k = 2
1188 *s*	CH_2 wag; k = 1
1125 *w*	ν(C–C) backbone/alkyl
1103 *vw*	ν(C–C) backbone/alkyl
1085 *m*	ν(C–C) side chains
1041 *w*	–
691 *s*	δ(-C–C–C-) backbone
495 *vw*	–
423 *w*	–

sh = shoulder; *w* = weak; *m* = medium; *s* = strong; *v* = very.

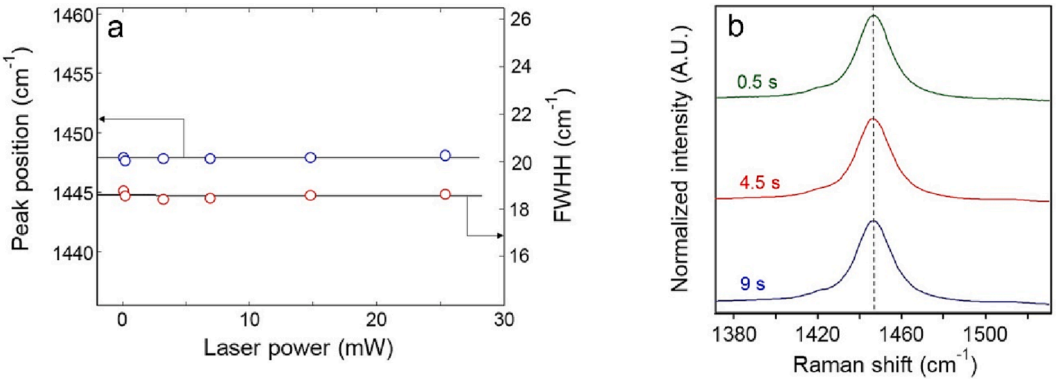

Fig. 5. (a): peak position (○) and *FWHH* (○) of the ν(–C=C–) peak as a function of the laser power. (b): the ν (–C=C–) peak collected at different exposure times with a laser power of 6.9 mW. Measurements performed at 301 K.

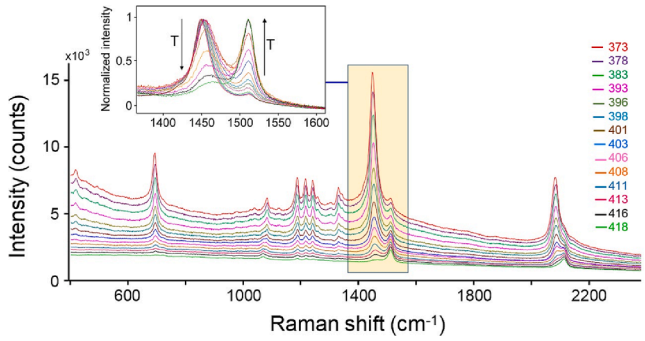

Fig. 7. SERS spectra of PNPs in the 373 – 418 K range. Temperatures as indicated. The inset highlights the 1380 – 1610 cm^{-1} frequency interval.

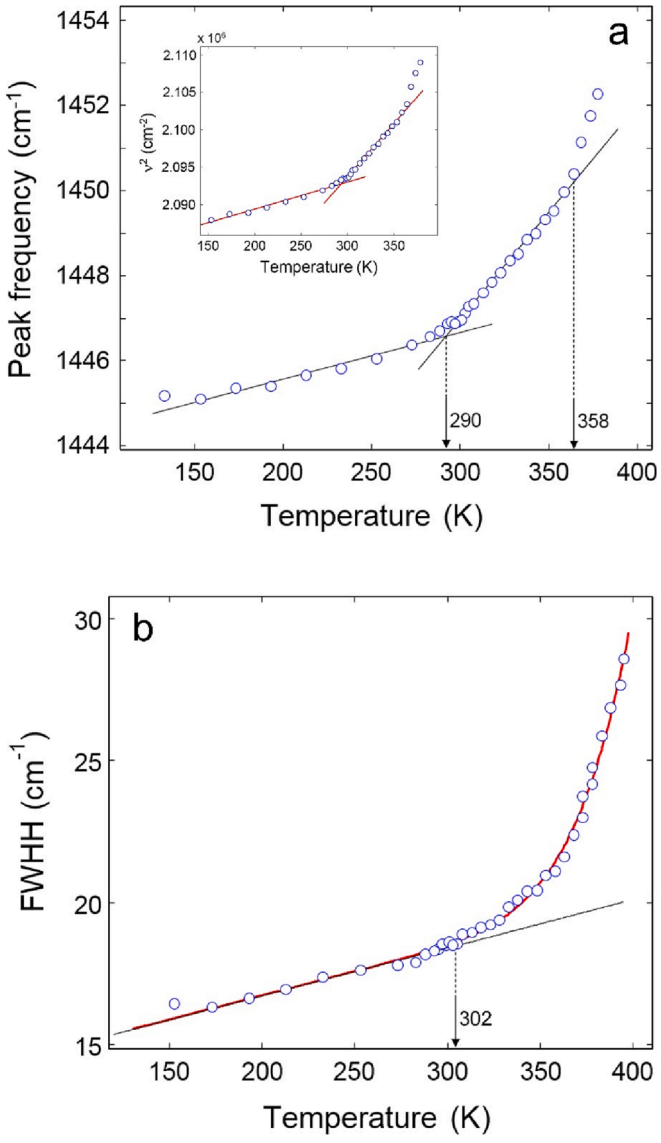

Fig. 8. Peak position (a) and FWHH (b) of the ν (–C=C–) mode of the blue-form as a function of temperature. In (a) red and black lines refer to the regression of the experimental data with Eqs. (2) and (3), respectively. In (b) the solid red curve is the regression obtained with eq. (6). (For interpretation of the references to color in this figure legend, the reader is referred to the web version of this article.)

$$\nu = \nu_0 \ [1 + \gamma^{'}(T - T_c)] \tag{3}$$

with $\gamma^{'} = \gamma/2$. Thus, the linear relationships are retained in a frequency vs temperature diagram, which represents the typical response function of a plasmonic thermosensor. Fig. 8a shows that, as a consequence of the phase transitions of the pPCDA shell, we observe a blue-shift of 5.5 cm^{-1} in going from 290 to 380 K, which represents a sensitivity comparable to the more recent values for adsorbate-based thermosensors [8,16]. Further advantages of the proposed nanostructure are a meaningful working range and a tight linearity of the response function in the range from the first to the second T_c ($T_c^{'} = 290K; T_c^{''} = 358K, R^2 = 0.995$). This relationship is theoretically predicted, which affords the transferability of the response function among different instrumental setups once the relevant parameters (γ and T_c) have been carefully measured. The identified linearity range is well suited for *in vivo* diagnostic applications [36]'.

The *FWHH* also displays a substantial increase with temperature, especially above 300 K (see Fig. 8b). Band broadening in an ordered molecular structure is due to anharmonicity and/or reorientation of molecules. When dynamic disorder prevails over the phonon decay process, the *FWHH* can be expressed as [31,32,37]:

$$FWHH = A + B{\cdot}T + C\left[\frac{\tau_c}{1 + \omega^2\tau_c^2}\right] \tag{4}$$

where the constant A accounts for broadening factors arising from structural and/or compositional defects [33,37], the linear term is related to the contribution of anharmonicity, and the third term represents the influence of the thermally activated reorientational process [33,34,37]. In particular, this term is characterized by the correlation time, τ_c, which is the average residence time in a given potential well, i. e. the time to jump from one potential well to another. It is given by:

$$\tau_c = \tau_0 \ e^{\frac{E_a}{k_B T}} \tag{5}$$

where E_a is the energy barrier to reorient the involved molecules and k_B is the Boltzmann constant. Since $\omega^2\tau_c^2 \ll 1$, eq. (4) can be rewritten as:

$$FWHH = A + B{\cdot}T + \tau_0 C e^{\frac{E_a}{k_B T}} \tag{6}$$

which affords to estimate E_a from the experimental data and verify the relaxation mechanism. The solid red line in Fig. 8b represents the regression of the experimental data points with eq. (6): it is found that the observed trend is well reproduced by the theory ($R^2 = 0.996$), which provides an E_a value of 10.9 kcal/mol, A = 13.4 cm^{-1}, and B = 0.017 K^{-1}. In Fig. 8b is also reported the contribution of the non-exponential terms of eq. (6) (solid black line); a comparison with the observed behavior reveals that structural/compositional defects (A) and anharmonicity (B) rule the broadening effect up to 302 K; afterward the molecular mobility is activated and the reorientation effect becomes predominant. The onset temperature to molecular mobility as estimated from the *FWHH* vs T curve is very close to the value of $T_c^{'}$ from the frequency vs T diagram (compare Fig. 7a and 7b), which confirms that the two spectroscopic parameters reflect the same physical transition, albeit with a different sensitivity. In fact, the broadening effect is not directly related to the thermal expansion, which makes it less responsive to phase changes and unable to capture the second transition involving the backbone chain. In terms of application as a plasmonic thermosensor, the *FWHH* increases by 10 cm^{-1} in going from 303 to 395 K, with an average sensitivity of 0.11 cm^{-1}/K, almost doubled in comparison to the peak position. Here again, the *a priori* knowledge of the analytical form of the response function and the availability of accurate B and E_a values will facilitate the construction of robust calibration curves.

Next, we considered the temperature dependence of the intensity, I, of the ν(–C = C–) vibration Preliminarily, we verified, by a deep-profile analysis in the −15 to 15 μm range, that the defocusing caused by the

temperature excursion during the VT-SERS run (3.0 μm, at most) does not affect the absolute intensity values (see Fig. 5S in SM). The I vs T trend is considerably more complex than those previously discussed are (see Fig. 9): a first linear decrease is followed by a sudden growth, a maximum at around 318 K and a further drop. This complexity is related to the plasmonic effect, which decays sharply with the distance, d, between the oscillator and the PNP surface. Theory predicts a power-law dependence of the form [38,39]:

$$EF = \frac{I}{I_0} \propto \left(\frac{R+d}{R}\right)^{-10} \tag{7}$$

where $EF = I/I_0$ is the enhancement factor (electromagnetic) and R is the radius of the spherical PNP. In practice, experimental values of the exponent range between −3.5 and −5.5 depending on the metal/adsorbate pair [40–42]. Thus, any expansion or contraction causing a change in the gap between the backbone chain and the metal surface will be immediately detected as a change in peak intensity.

The slight linear decrease in the 150 – 290 K range suggests that in this interval, the system is dimensionally stable and the peak intensity is ruled by the ordinary temperature dependence of the inelastic light scattering [35,43]. At 290 K the steep increase reflects the phase transition detected by peak position and FWHH; the increment suggests a reduction of the distance between the backbone and the PNP surface, likely caused by the expansion of the layer formed by the external alkyl substituents [the $(CH_2)_{11}CH_3$ groups]. This expansion apparently stops at around 320 K, followed by a pseudo-stationary regime that almost parallels the one at low temperatures. Starting from 355 K (the T_c'' temperature from peak position measurements) the intensity drops abruptly (see also Fig. 7) with a 70 % reduction in around 30 K. At T_c'' emerges the red-form, causing a substantial modification of the localized surface plasmon resonance (LSPR) band. In fact, in passing from the blue to the red-form the shape of the UV–VIS spectrum changes substantially, and the maximum moves from 650 to 540 nm [22,44–46]. In this light, we associate the final intensity drop to an off-resonance effect, i.e. a mismatch between the excitation line at 638 nm and the LSPR, taking place when the blue-form converts into the red.

In summary, the VT-SERS measurements demonstrate that the sensitivity of the peak intensity towards any dimensional modification of the polymer shell makes it unsuitable as a parameter to be employed in plasmonic thermosensing. On the other hand, this same sensitivity renders the SERS intensity of selected signals a powerful tool for investigating volume contraction/expansion and the associated phase transitions for any polymeric shell that can be made to surround a plasmonic core.

According to eq. (7), if the absolute intensity depends strongly on d, the intensity ratio between two SERS peaks corresponds to the ratio between their Raman counterparts, assuming a frequency-independent enhancement. This condition is satisfied for the doublet at 1447–1512 cm^{-1} due to the small frequency gap. Thus, we can assume, according to the general theory of inelastic light scattering [43,47], that $I_{1512}/I_{1447} = \omega_{1512}/\omega_{1447} \bullet C_{RF}/C_{BF}$ with C_{RF} and C_{BF} denoting the concentration of the red and the blue form, respectively, while ω_i are the Raman cross-sections of the respective signals. More specifically, C_{RF} and C_{BF} represent the concentration of conformational sequences generating the two peaks. According to a detailed *ab-initio* investigation on the structural properties of pPCDA [48] the blue and the red sequences are characterized, respectively, by diacetylenic conformations with a dihedral angle, τ, of 170° and 145° (see Fig. 7S in SM).

The conversion between the two forms: $BF \leftrightarrows RF$is regulated by the equilibrium constant $K_{eq} = C_{RF}/C_{BF}$. The van't Hoff equation for K_{eq} is:

$$ln\left(\frac{I_{1512}}{I_{1447}}\right) = -\frac{\Delta H}{RT} + \frac{\Delta S}{R} + K \tag{8}$$

where the symbols have the usual meaning and K is a constant accounting for the ratio between the Raman cross-sections of the two signals. Fig. 10 reports the I_{1512}/I_{1447} ratio as a function of temperature, which marks the onset of conversion at 358 K, the T_c'' temperature (see Fig. 8a). The van't Hoff diagram, represented in the inset of Fig. 10, displays the negative slope characteristic of an endothermic process, and a ΔH value of – (11 ± 1.3) kcal/mol. This figure is coincident with the E_a value obtained from the *FWHH* vs T diagram (10.9 kcal/mol), which confirms the soundness of the band-broadening approach in evaluating the activation energy of the transition and demonstrates that the process is enthalpically driven. The above analysis also demonstrates that VT-SERS measurements can be a sensitive and accurate method to investigate conformational equilibria in thin polymer films adsorbed on plasmonic surfaces.

4. Conclusions

In the present contribution we introduce a novel approach to plasmonic thermosensing, based on the phase transition of the external layer of a core–shell nanostructure. We have synthesized and tested poly

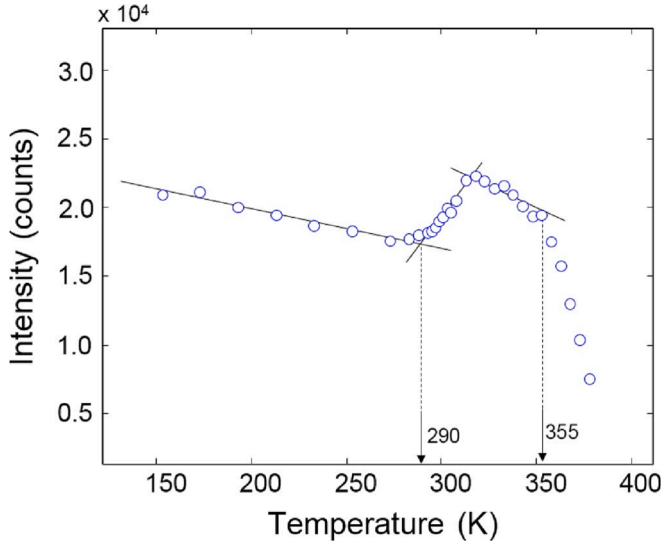

Fig. 9. Intensity (peak height) of the ν (–C=C–) mode of the blue-form as a function of temperature. (For interpretation of the references to color in this figure legend, the reader is referred to the web version of this article.)

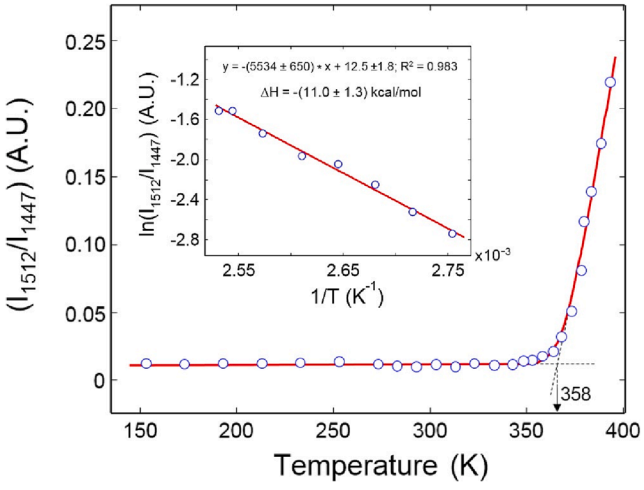

Fig. 10. The ratio between the intensities of the peaks at 1512 and 1447 cm^{-1} as a function of absolute temperature. The inset displays the van't Hoff plot of the intensity ratio.

((10,12-pentacosadiynoic acid)-coated gold nanospheres (pPCDA@AuNPs), which exhibit significant and reproducible temperature effects that can be accurately quantified by SERS spectroscopy. The following conclusions can be drawn:

- The PCDA outer shell has been polymerized *in situ* in the blue form, which is a metastable phase. Upon heating above 290 K, a transition in the stable red form takes place, causing an increase in the position and the *FWHH* of the ν(–C = C–) peak. These effects can be theoretically predicted.
- The response functions of both the above parameters afford a proper temperature sensitivity and a working range suitable for *in vivo* and *in vitro* diagnostic applications of the proposed thermosensor.
- The *a priori* knowledge of the analytical form of the response functions facilitates the construction of accurate and transferable calibration curves.
- The intensity of the ν(–C = C–) peak is also very sensitive to the phase transitions but its behavior is complex and unsuitable for temperature sensing.
- It is also demonstrated that VT-SERS measurements are a powerful tool to investigate the behavior of ultrathin polymer films (down to the single molecular layer) surrounding plasmonic nanoparticles. These films are of major technological interest in the semi-conductor, optoelectronic, manufacturing and biomedical industries.

Declaration of Competing Interest

The authors declare that they have no known competing financial interests or personal relationships that could have appeared to influence the work reported in this paper.

Data availability

Data will be made available on request.

Appendix A. Supplementary material

Supplementary data to this article can be found online at https://doi.org/10.1016/j.apsusc.2023.157799.

References

[1] M.L. Brongersma, N.J. Halas, P. Nordlander, Plasmon-induced hot carrier science and technology, Nat. Nanotechnol. 10 (2015) 25–34.
[2] J. Lee, S. Mubeen, X. Ji, G.D. Stucky, M. Moskovits, Plasmonic photoanodes for solar water splitting with visible light, Nano Lett 12 (2012) 5014–5019.
[3] S. Mubeen, J. Lee, N. Singh, S. Krämer, G.D. Stucky, M. Moskovits, An autonomous photosynthetic device in which all charge carriers derive from surface plasmons, Nat. Nanotechnol. 8 (2013) 247–251.
[4] S. Mukherjee, F. Libisch, N. Large, O. Neumann, L.V. Brown, J. Cheng, J.B. Lassiter, E.A. Carter, P. Nordlander, N.J. Halas, Hot electrons do the impossible: plasmon-induced dissociation of H2 on Au, Nano Lett 13 (2013) 240–247.
[5] P. Christopher, H. Xin, S. Linic, Visible-light-enhanced catalytic oxidation reactions on plasmonic silver nanostructures, Nat. Chem. 3 (2011) 467–472.
[6] S. Linic, P. Christopher, D.B. Ingram, Plasmonic-metal nanostructures for efficient conversion of solar to chemical energy, Nat. Mater. 10 (2011) 911–921.
[7] L. Dykman, N. Khlebtsov, Gold nanoparticles in biomedical applications: recent advances and perspectives, Chem. Soc. Rev. 41 (2012) 2256–2282.
[8] S. Hu, B.-J. Liu, J.-M. Feng, C. Zong, K.-Q. Lin, X. Wang, D.-Y. Wu, B. Ren, Quantifying surface temperature of thermoplasmonic nanostructures, J. Am. Chem. Soc. 140 (2018) 13680–13686.
[9] K. Okabe, N. Inada, C. Gota, Y. Harada, T. Funatsu, S. Uchiyama, Intracellular temperature mapping with a fluorescent polymeric thermometer and fluorescence lifetime imaging microscopy, Nat. Commun. 3 (2012) 1–9.
[10] T. Vo-Dinh, H.-N. Wang, J. Scaffidi, Plasmonic nanoprobes for SERS biosensing and bioimaging, J. Biophotonics 3 (2010) 89–102.
[11] M.K. Gregas, J.P. Scaffidi, B. Lauly, T. Vo-Dinh, Surface-enhanced raman scattering detection and tracking of nanoprobes: Enhanced uptake and nuclear targeting in single cells, Appl. Spectrosc. 64 (2010) 858–866.
[12] S.L. Kleinman, R.R. Frontiera, A.-I. Henry, J.A. Dieringer, R.P. Van Duyne, Creating, characterizing, and controlling chemistry with SERS hot spots, PCCP 15 (2013) 21–36.
[13] M.-C. Daniel, D. Astruc, Gold nanoparticles: assembly, supramolecular chemistry, quantum-size-related properties, and applications toward biology, catalysis, and nanotechnology, Chem. Rev. 104 (2004) 293–346.
[14] Y. Fang, N.-H. Seong, D.D. Dlott, Measurement of the distribution of site enhancements in surface-enhanced raman scattering, Science 321 (2008) 388–392.
[15] K.-H. Yang, F.-D. Mai, C.-C. Yu, Y.-C. Liu, Room-temperature sensor based on surface-enhanced Raman spectroscopy, Analyst 139 (2014) 5164–5169.
[16] Y. Lu, L.-W. Wu, W. Cao, Y.-F. Huang, Finding a sensitive surface-enhanced Raman spectroscopic thermometer at the nanoscale by examining the functional groups, Anal. Chem. 94 (2022) 6011–6016.
[17] T. Jiang, X. Wang, J. Zhou, H. Jin, The construction of silver aggregate with inbuilt Raman molecule and gold nanowire forest in SERS-based immunoassay for cancer biomarker detection, Sens. Actuat. B 258 (2018) 105–114.
[18] S. Tang, H. Liu, M. Wang, S. Wang, C. Wang, C. Gu, Z. Zhao, T. Jiang, J. Zhou, Further enhancement of SERS signals from Au@ Ag@ PSPAA core–shell nanoparticles surrounded by ag nanoplates, Mater. Chem. Phys. 225 (2019) 60–63.
[19] M. Alloisio, S. Zappia, A. Demartini, M.I.M. Espinoza, M. Ottonelli, G. Dellepiane, S. Thea, O. Cavalleri, R. Rolandi, Silver-polydiacetylene core–shell nanohybrids: from nano to mesoscale architectures, Nano-Struct. Nano-Objects 4 (2015) 15–22.
[20] M. Ottonelli, S. Zappia, A. Demartini, M. Alloisio, Chitosan-stabilized noble metal nanoparticles: study of their shape evolution and post-functionalization properties, Nanomaterials 10 (2020) 224.
[21] J.M. Kim, Y.B. Lee, S.K. Chae, D.J. Ahn, Patterned color and fluorescent images with polydiacetylene supramolecules embedded in poly (vinyl alcohol) films, Adv. Funct. Mater. 16 (2006) 2103–2109.
[22] M.I. Martinez-Espinoza, M. Maccagno, S. Thea, M. Alloisio, Self-assembly and photopolymerization of a novel quaternary-ammonium functionalized diacetylene on noble metal nanoparticles: a comparative study, Appl. Surf. Sci. 427 (2018) 724–732.
[23] J. He, S. Unser, I. Bruzas, R. Cary, Z. Shi, R. Mehra, K. Aron, L. Sagle, The facile removal of ctab from the surface of gold nanorods, Colloids Surf. B Biointerfaces 163 (2018) 140–145.
[24] M. Castellano, M. Alloisio, R. Darawish, A. Dodero, S. Vicini, Electrospun composite mats of alginate with embedded silver nanoparticles, J. Therm. Anal. Calorim. 137 (2019) 767–778.
[25] D.W. Marquardt, Finite difference algorithm for curve fitting, J. Soc. Ind. Appl. Math. 11 (1963) 431–441.
[26] J. Pitha, R.N. Jones, A comparison of optimization methods for fitting curves to infrared band envelopes, Can. J. Chem. 44 (1966) 3031–3050.
[27] N.R. Jana, L. Gearheart, C.J. Murphy, Seed-mediated growth approach for shape-controlled synthesis of spheroidal and rod-like gold nanoparticles using a surfactant template, Adv. Mater. 13 (2001) 1389–1393.
[28] G. Baffou, R. Quidant, Thermo-plasmonics: using metallic nanostructures as nano-sources of heat, Laser Photonics Rev. 7 (2013) 171–187.
[29] K. Seto, Y. Hosoi, Y. Furukawa, Raman spectra of langmuir-blodgett and langmuir-schaefer films of polydiacetylene prepared from 10, 12-pentacosadiynoic acid, Chem. Phys. Lett 444 (2007) 328–332.
[30] R. Aroca, Surface-enhanced vibrational spectroscopy, John Wiley & Sons, England, 2006.
[31] C. Carabatos-Nédelec, P. Becker, Order–disorder and structural phase transitions in solid-state materials by Raman scattering analysis, J. Raman Spectrosc 28 (1997) 663–671.
[32] F. Jebari, P. Becker, C. Carabatos-Nédelec, Order-disorder phase transition in diethylenetriammonium chlorocadmate single crystals determined by Raman spectroscopy, J. Raman Spectrosc. 25 (1994) 261–265.
[33] M. Mączka, A. Gągor, B. Macalik, A. Pikul, M. Ptak, J. Hanuza, Order-disorder transition and weak ferromagnetism in the perovskite metal formate frameworks of [(CH3)2NH2][M(HCOO)3] and [(CH3)2ND2][M(HCOO)3] M = Ni, Mn, Inorg Chem 53 (2014) 457–467.
[34] A.A. da Costa, A. Amado, M. Becucci, C. Kryschi, Order-disorder phase transition in p-terphenyl and p-terphenyl: tetracene doped crystals as studied by raman spectroscopy, J Mol Struct 416 (1997) 69–73.
[35] P.d.R. Andrade, S.P.S. Porto, Hard core phonon frequency at transition temperature, Solid State Communications, 14 (1974) 547-550.
[36] Q. Li, H. Huo, Y. Wu, L. Chen, L. Su, X. Zhang, J. Song, H. Yang, Design and Synthesis of SERS Materials for In Vivo Molecular Imaging and Biosensing, Advanced Science, n/a 2202051.
[37] P.d.R. Andrade, S. Porto, On linewidth of phonons associated to a disorder mechanism, Solid State Communications, 13 (1973) 1249-1254.
[38] C.A. Murray, in: R.K. Chang, Furtak, T. E. (Ed.) Surface Enhanced Raman Scattering, Plenum Press, New York, 1982, pp. 208.
[39] B. Kennedy, S. Spaeth, M. Dickey, K. Carron, Determination of the distance dependence and experimental effects for modified sers substrates based on self-assembled monolayers formed using alkanethiols, J. Phys. Chem. B 103 (1999) 3640–3646.
[40] F.M. Liu, P. Köllensperger, M. Green, A. Cass, L. Cohen, A note on distance dependence in surface enhanced Raman spectroscopy, Chem Phys Lett 430 (2006) 173–176.
[41] Q. Ye, J. Fang, L. Sun, Surface-enhanced Raman scattering from functionalized self-assembled monolayers. 2. Distance dependence of enhanced Raman scattering from an azobenzene terminal group, J. Phys. Chem. B 101 (1997) 8221–8224.
[42] J. Gersten, A. Nitzan, Electromagnetic theory of enhanced Raman scattering by molecules adsorbed on rough surfaces, J. Chem. Phys. 73 (1980) 3023–3037.
[43] D.A. Long, Raman Spectoscopy, McGraw-Hill, New York, 1977.
[44] R.E. Martin, F. Diederich, Linear monodisperse π-conjugated oligomers: model compounds for polymers and more, Angew. Chem. Int. Ed. 38 (1999) 1350–1377.

[45] H. Meier, Conjugated oligomers with terminal donor–acceptor substitution, Angew. Chem. Int. Ed. 44 (2005) 2482–2506.
[46] M. Gholami, R.R. Tykwinski, Oligomeric and polymeric systems with a cross-conjugated π-framework, Chem Rev 106 (2006) 4997–5027.
[47] R.L. McCreery, Photometric Standards for Raman Spectroscopy, in: J.M. Chalmers, P.R. Griffiths (Eds.), Handbook of vibrational spectroscopy, Wiley, Chichester, U. K., 2002, pp. 920–932.
[48] C. Gellini, M. Muniz-Miranda, P.R. Salvi, M. Alloisio, G. Dellepiane, Structural properties of photochromic polyPCDA: a computational study, J Mol Struct 993 (2011) 435–437.